Version of record at: https://doi.org/10.1149/1945-7111/ac8b3d

Journal of The Electrochemical Society, 2022 **169** 090518

Polysulfide Speciation in Li–S Battery Electrolyte via In-Operando Optical Imaging and Ex-Situ UV-vis Spectra Analysis

Gbenga S. Taiwo,[1] Ali Rashti,[1] Mritunjay Mishra,[2] and Koffi P. C. Yao[1,*,z]

[1]*Department of Mechanical Engineering, University of Delaware, Newark, Delaware, United States of America*
[2]*Department of Chemistry and Biochemistry, University of Delaware, Newark, Delaware, United States of America*

Lithium sulfur (Li–S) batteries have received significant attention as one of the energy storage systems with excellent prospects for emerging applications due to their high energy density and low-cost. However, there are fundamental challenges impeding the commercialization of Li–S batteries. Notorious among those challenges is the "polysulfide shuttle" consisting of the dissolution into the electrolyte solvent and subsequent crossover to the anode of long-chain lithium polysulfides. Sparingly solvating electrolytes have been exploited as an approach to reduce the dissolution of polysulfides and thereby the shuttle effect. Using an optical in operando lithium-sulfur cell and ex situ UV–vis spectroscopy, we elucidate the speciation of polysulfides in fully and sparingly solvating electrolytes for Li–S batteries. Extensive literature meta-analysis reveals that the most unambiguous effect of sparingly solvating solvent is in improving the coulombic efficiency of sulfur-cells. Experimental optical imaging and UV–vis characterization elucidate a shift towards shorter-chain polysulfides in electrolytes with increasing lithium-salt concentration (more sparingly solvating). The shift to shorter-chain polysulfides corresponds to a reduction of polysulfide species participating in shuttling which corroborate the increased coulombic efficiency in sparingly-solvating electrolytes.

Manuscript submitted May 24, 2022; revised manuscript received August 10, 2022. Published September 13, 2022.

Supplementary material for this article is available online

Advances in electrochemical energy storage have helped in the transformation of portable electronics, development of electric vehicles, and stationary electric power storage devices. Lithium-ion batteries (LIBs) have taken the lead among portable electrochemical energy storage devices. However, the state-of-the-art intercalation cathode materials such as $LiCoO_2$ and $LiFePO_4$ are approaching their theoretical capacity (170–270 mAh·g^{-1}) which is insufficient to meet the rapidly growing demand for cost-effective high-energy storage.[1–7] Thus, efforts are being intensified towards the development of batteries with higher energy density and reduced cost per watt-hours.[8–10] Among the many promising candidates for next-generation electrochemical energy storage systems, lithium-sulfur batteries (LSBs) have received immense interest due to their high theoretical specific capacity (1675 mAh·g^{-1}) and theoretical energy density (2600 Wh·kg^{-1}).[7,11–14] Sulfur is abundant, extremely low cost, and easily available as leftover byproduct of fossil fuel refinement. Their relatively low redox potential (2.1–2.4 V vs Li/Li^+) notwithstanding, LSBs have the capacity to attain higher gravimetric and volumetric energy densities compared to other lithium-ion chemistries.[15] Unlike LIBs which in practice thus far are limited to one electron per host molecular/crystallographic unit, LSB can accommodate up to two electrons per sulfur atom.[2,7]

The simplest LSB arrangement consists of a lithium metal anode, a separator filled with an electrolyte which serves as a medium for lithium-ion transport, and the sulfur cathode. LSBs undergo precipitation-dissolution type chemistry and have inherent challenges such as the large volume change in the sulfur cathode during repeated cycling, the electronic and ionic insulating nature of sulfur and lithium sulfides, the polysulfide shuttle (LiPS-shuttle), and lithium dendrite growth at the anode during lithium plating.[16–21] The LiPS-shuttle in particular has thwarted progress in the development of the chemistry since its discovery in the 1960s. In order to overcome this challenge and improve LSBs performance, sulfur cathode architecture has been modified to trap polysulfides as soon as they are formed,[22–27] separators are coated with extra layer for physical confinement or chemical adsorption of polysulfides,[28–31] electrolytes are tuned and rational formulation are being pursued.[18]

The electrolyte is perhaps the most important component of LSB as it largely influences the dissolution and diffusion of polysulfides between the electrodes.[32] An electrolyte that would find application in LSB should be stable against the very reactive lithium anode and sulfur cathode. In addition, it should be a good ionic conductor, have a wide potential window and should be thermally stable.[33] However, the reactive nature of lithium polysulfide (LiPS) is limiting the solvents and lithium salts combination that can be explored for designing more efficient novel electrolytes for LSB.[32,34]

The conventional or baseline electrolyte is 1 M lithium bis (trifluoromethanesulfonyl)imide (LiTFSI) in equal volume of 1,3-dioxolane (DOL) and 1,2-dimethoxyethane (DME). This is a type of fully-solvating electrolyte (FSE, Table I). The salt concentration is relatively low (vs the saturation concentration of ca. 7 M) leaving plenty of solvation overhead to solubilize lithium polysulfide (LiPS). The full solvation of LiPS allows maximum utilization of the active material and promote reaction kinetics. The accepted reaction sequence is as shown:

$$S_8 \rightarrow Li_2S_{8(l)} \rightarrow Li_2S_{6(l)} \rightarrow Li_2S_{4(s+l)} \rightarrow Li_2S_{2(s)} \rightarrow Li_2S_{(s)} \quad [1]$$

Unfortunately, full solvation of LiPS enables it to crossover to the anode (lithium), leading to the deposition of Li_2S on the lithium-anode surface, passivation of the anode, and continuous permanent loss of active sulfur. This phenomenon chiefly manifests as unsatisfactory capacity retention over prolonged cycles in cells with dilute electrolytes. This drawback has spurred efforts to carefully formulate electrolytes that will provide good cycle life, efficient capacity retention and better rate capability. Sparingly solvating electrolytes (SSEs) are one of the most promising electrolyte systems (Table I) that the effort has yielded.[16,17] In sparingly-solvating electrolytes, the solvent is (nearly) salt-saturated leaving minimal solvation overhead for LiPS dissolution and the reaction pathway should favor shorter chain polysulfides via early supersaturation on the electrode surface.[35]

$$S_8 \rightarrow [Li_2S_8 \rightarrow Li_2S_6]_{transitory} \rightarrow Li_2S_{4(s+l)} \rightarrow Li_2S_{2(s)}/Li_2S_{(s)} \quad [2]$$

*Electrochemical Society Member.
zE-mail: claver@udel.edu

Version of record at: https://doi.org/10.1149/1945-7111/ac8b3d

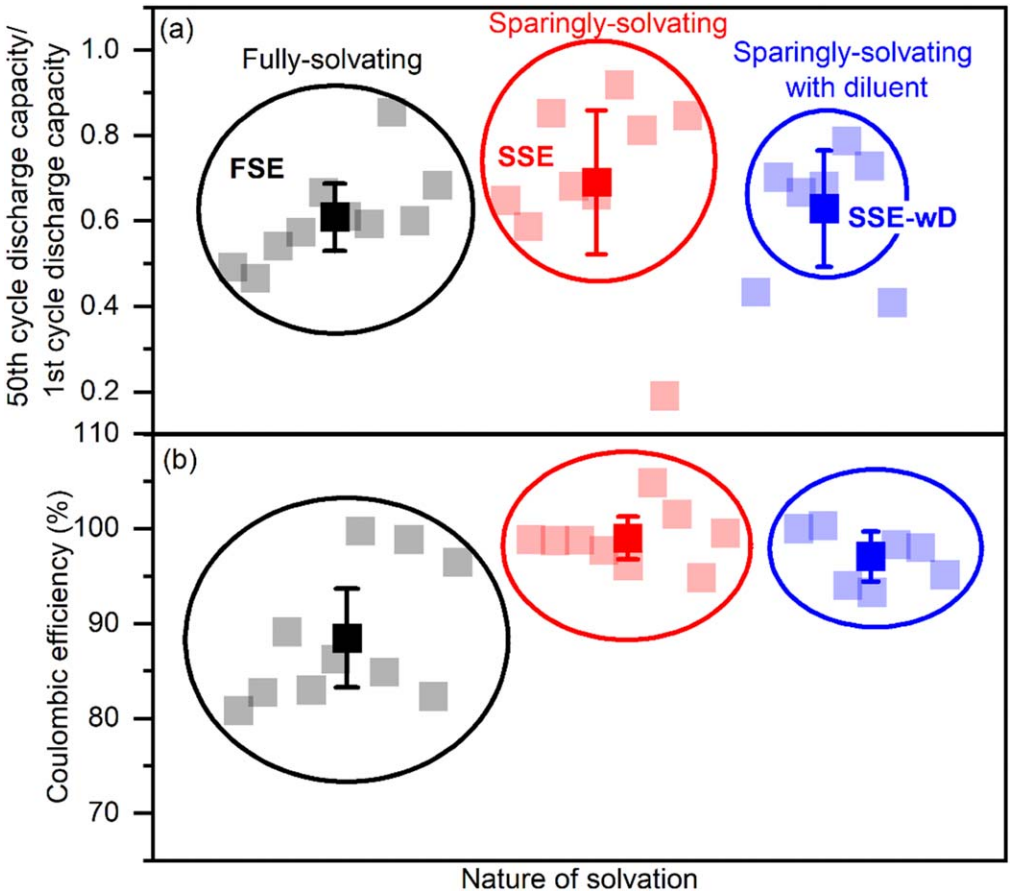

Figure 1. Summary of literature-reported performance of LSBs using electrolytes classified as fully-solvating, sparingly-solvating, and sparingly-solvating with diluent.[16,36,37,39,42–52]

Some benefits of this system include minimization of LiPS solvation, reduction of the amount of LiPS crossover to the anode, reduction of active sulfur loss, and reduced sulfides passivation of the anode. These benefits become evident in the capacity retention that is achieved when SSE are employed in Li–S batteries. SSEs are formulated either by saturating the solvent with lithium salt[32,36–38] or by combining non-polar solvents with specially prepared lithium salts with low-ion pairing.[37,39] However, high salt concentration increases the viscosity of the electrolyte which adversely affects the Li^+ cation transport reducing the electrolyte conductivity.[36] Consequently, cell polarization is increased especially when cycled at room temperature. Viscosity can be reduced, and redox kinetics improved by raising the operating temperature or by adding a cosolvent.[37,40–43] Cosolvent such as 1,1,2,2-tetrafluoroethyl-2,2,3,3-tetrafluoropropyl ether (TTE)[41] (Table I) serves as a diluent which reduces viscosity, increasing ionic conductivity without significantly impacting polysulfide solubility maintaining its sparingly-solvating property (SSE-wD). It is worth noting that the nature of the Li-salt (the Lewis basicity of the coordinating anion) in the electrolyte formulation has been shown to significantly impact the achievable saturation concentration as well as the polysulfide solubility in the electrolyte.[32]

To provide a generalizable view of the effect of the solvent categories discussed above, we compiled the performances of different Li–S electrolyte systems reported in 15 publications where the cell was cycled for at least 50 cycles (Fig. 1). The references, electrolyte compositions, and the conditions of cycling are listed in the supporting information (Table SI). Although there are some variations in applied current density and salt used, most studies considered used an applied rate of ca. 0.1–0.2 C and Lithium bis(trifluoromethylsulfonyl)imide (LiTFSI) as the salt. We normalized the capacity retention to the initial capacity to account for those variations in experimental conditions. A general

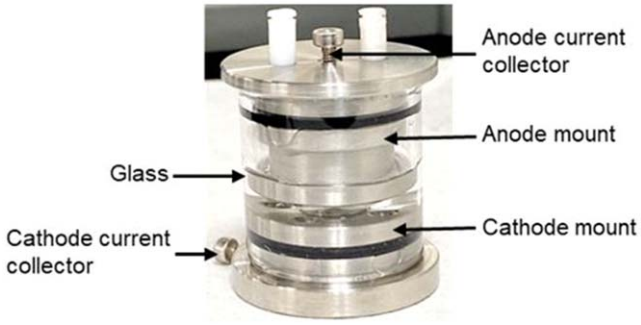

Figure 2. Fabricated in-operando lithium-sulfur cell.

improvement in the normalized capacity retention (50th cycle vs 1st cycle) and coulombic efficiency from FSE to SSE electrolytes is observed (Fig. 1a). The calculated averages of ratios of 50th to 1st cycle capacities from FSE to SSE to SSE-wD are 0.61, 0.69, and 0.63 respectively. The 50-cycle-averaged coulombic efficiency show group-averages of 88, 99, and 97% from FSE to SSE to SSE-wD (Fig. 1b). The greater capacity retention and coulombic efficiency of SSEs has been attributed to reduced loss of active sulfur to LiPS crossover;[36,37] greater retention of active material pushes the capacity retention to 0.69 on average for the SSE literature we reviewed compared to 0.61 and 0.62 for FSE and SSE-wD. Assessing the normalized capacity retention of SSE-wDs wherein diluent co-solvents are added to concentrated SSEs to reduce viscosity and ionic resistance, a drop in the capacity retention vs the parent SSEs is evident as depicted by the blue data points in Fig. 2a.

We postulate that some solvent molecules are freed for partial solvation of LiPS when adding the diluent which causes some level of

shuttling of LiPS to the anode side. This postulate matches with a corresponding slight drop in the average coulombic efficiency (97% for SSE-wDs vs 99% for undiluted SSEs).

More importantly, there is statistically-significant overlap between the nominally-improved capacity retention of sparingly-solvating electrolytes and the nominally-lower capacity retention of fully-solvating solvent in Fig. 1. Thereby, it is paramount to improve the empirical understanding of the electrochemical behavior of the two electrolyte systems in a more systematic fashion under the same laboratory conditions. Techniques that have been used to investigate polysulfide speciation in electrolytes of LSBs include UV–vis spectroscopy,[53–56] Raman spectroscopy,[57–61] FT-IR spectroscopy,[62,63] X-ray absorption spectroscopy,[34] and optical image analysis[64,65] but not yet under unified combination of electrolyte solvation level and electrochemical sulfur cycling conditions. Herein, we combine optical imaging in operando and ex situ UV–vis spectra analysis to systematically elucidate polysulfide speciation from dilute (fully solvating, FSEs) towards concentrated electrolyte (sparingly solvating, SSEs). We focus on the region of 0–212 $mAh{\cdot}g^{-1}_{S}$ where the soluble polysulfides are dominant species to elucidate the behavior of concentration on LiPS dissolution into the electrolyte. Investigation of the behavior of SSE-wDs as well as the solid-polysulfides region of 250–1675 $mAh{\cdot}g^{-1}_{S}$ is underway and will be reported at a future date.

Experimental

Operando lithium-sulfur cell design.—Our operando lithium-sulfur cell is shown in Fig. 2. It consists of quartz glass body to allow visualization, two stainless steel blind flanges for mounting the electrodes, and two stainless steel screws which serve as current collectors. A gap of 5 mm between the anode and cathode mounts is reserved for the electrolyte bridge between the electrodes.

Preparation of S/C composite cathode.—The sulfur composite cathode was prepared by mixing 70 wt% elemental sulfur (99.5%, Thermo Scientific), 20 wt% Super P carbon black (99+% metal basis, Thermo Scientific) and 10 wt% polyvinylidene fluoride (Thermo Scientific). The powder mixture is ball-milled at 300 rpm for approximately 90 min at room temperature. The resulting mixture was dispersed in N-methyl-2-pyrrolidone (99.5% anhydrous, Sigma-Aldrich) to form a homogenous slurry. The slurry was coated on aluminum foil with areal loading of 1.96 $mg{\cdot}cm^{-2}$ and dried at 60 °C under vacuum overnight. Electrode samples one centimeter in diameter were punched for cell assembly.

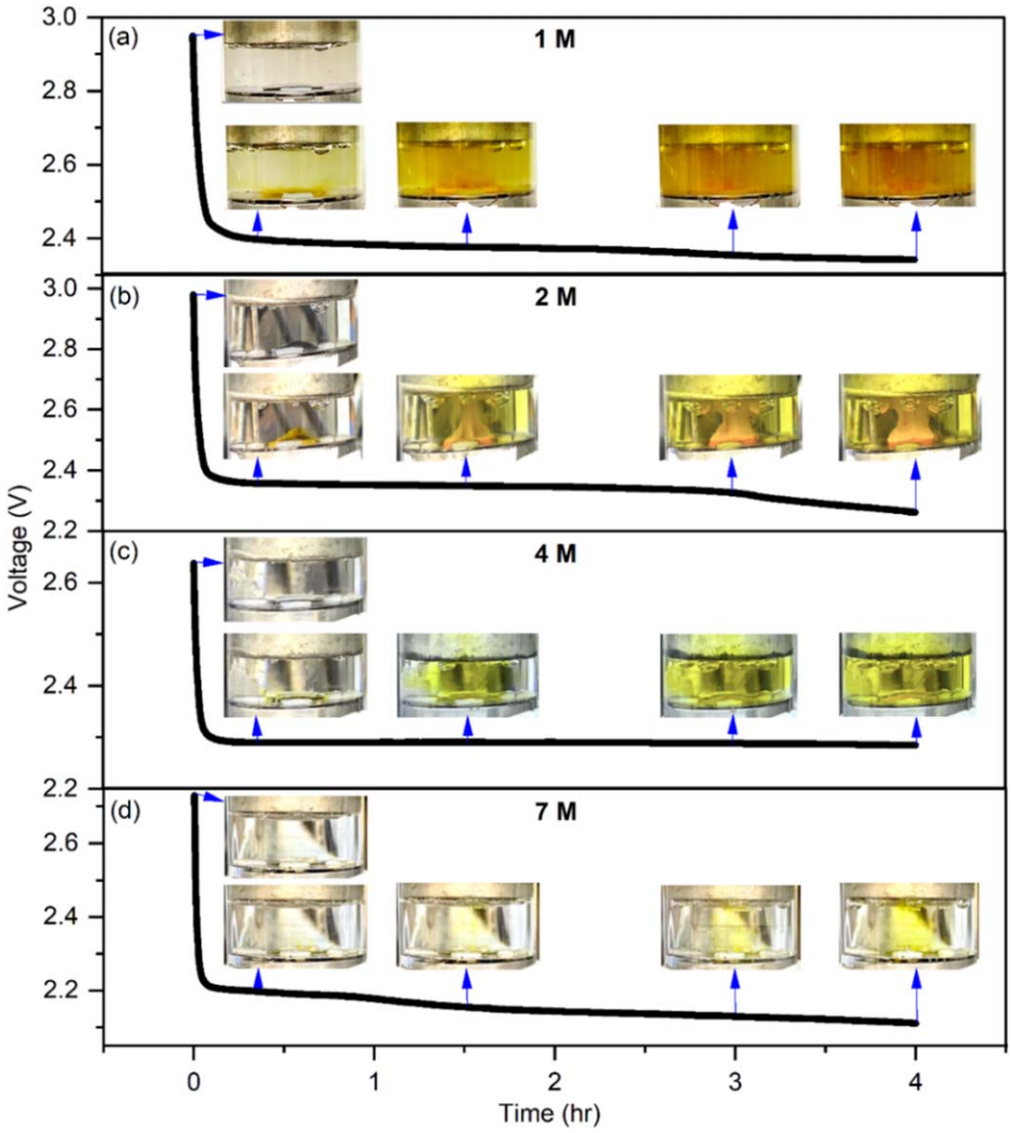

Figure 3. The galvanostatic discharge profile of 1, 2, 4 and 7 M LiTFSI in DOL:DME (1:1 by vol.) at a current rate of C/30.

Preparation of electrolyte.—The electrolyte was prepared by dissolving lithium bis(trifluoromethanesulfonyl)imide (99.95% trace metal basis, Sigma-Aldrich) in conventional 1:1 volume ratio of 1,3-dioxolane (99.8%, Sigma-Aldrich) and 1,2-dimethoxyethane (99.9%, Sigma-Aldrich) with 2 wt% lithium nitrate (99.99%, Sigma-Aldrich) additive. The electrolyte was prepared at concentrations of 1, 2, 4, and 7 M (saturated) to systematically span the spectrum of fully-solvating to sparingly solvating electrolyte systems.

Electrochemical measurements of the operando lithium-sulfur cell.—The operando lithium sulfur cell was assembled in an argon-filled box ($H_2O < 1$ ppm, $O_2 < 1$ ppm). Sulfur electrode was placed on the cathode mount, secured with a screw-fastened thin circular clamp, and the arrangement is inserted into the quartz glass. Electrolyte is then added and the anode mount with lithium foil is placed on top of the electrolyte layer to seal the cell. Electrochemical cycling was performed on the assembled cell using a Gamry Reference 3000 Potentiostat/Galvanostat/ZRA at a rate of C/30 ($I = 80\ \mu$A) between a voltage range of 1–3.5 V (vs Li/Li^+) at room temperature. The measurement was constrained to the region of the first plateau of a typical lithium-sulfur cell using 1 M LiTFSI in DOL:DME (1:1, by vol); the capacity is limited to $\sim$200 mAh·g^{-1} where the LiPS-shuttle is of the most concern. Optical images of the cell were collected automatically at 10 min intervals using a camera.

UV–vis measurements.—The ex situ UV–vis measurement was carried out using an Agilent Cary 60 UV–vis Spectrophotometer which was switched on for about 20 min before the measurement. The measurement was taken at the end of the first discharge, and a scan rate of 60 nm min^{-1} was selected so that high-quality signals can be obtained. The range of 200 nm to 800 nm was scanned in $\sim$10 min.

Results and Discussion

Electrochemical performance of the operando cell.—The cell was cycled slowly at a rate of C/30 to allow the capture of detailed quasi real-time images of the galvanostatic discharge and charge processes. During the cycling of the cell, we observed that the reduction of sulfur to lithium polysulfide begins around 20 min ($\sim$10 mAh g_{sulfur}^{-1}) into the discharge cycle (Fig. 3) for all the different salt concentrations (1, 2, 4, and 7 M).

In the 1 M LiTFSI concentration electrolyte (fully-solvating, FSE), by $t = 20$ min, a plume of deep-orange colored sulfur products is visible and rise (against gravity) from the sulfur electrode rapidly spreading in the electrolyte towards lithium anode above the sulfur electrode. By $t = 1.5$ h ($\sim$80 mAh g_{sulfur}^{-1}), the electrolyte has turned deep-orange with a steady outflow of soluble sulfur species from the electrode into the electrolyte. Excessive crossover of lithium polysulfide to the anode is evident. The color of the electrolyte changes from clear to deep-orange at the end of 4 h discharge ($\sim$220 mAh g_{sulfur}^{-1}). This confirms the generation, conversion, and shuttling of soluble polysulfide species that takes place in the first plateau of a typical dilute electrolyte LSB. Similar results were reported by Sun et al.[64] using similar optical monitoring.

Increasing the LiTFSI concentration to 2 M (anticipated decrease of solvation-capacity for LiPSs compared to 1 M), lighter-orange sulfur products emerge from the electrode at $t = 20$ min that remain nominally attached to the sulfur electrode (Fig. 3b); the electrolyte remains clear. Continued discharge to $t = 1.5$ h displays a self-sticking string of light-orange LiPSs that disperses much slower in the electrolyte compared to the case of 1 M. This string of LiPSs crosses the 5 mm electrolyte gap to reach the lithium anode surface above where it spreads circularly in a "geyser" pattern. This LiPSs "geyser" pattern continues until the end of the 4 h discharge whence the electrolyte at large adopts a light-orange coloring. This experiment with the 2 M electrolyte was repeated several times to ascertain the unusual polysulfide "geyser" pattern observed. It is clear from the differing color and plume behavior between the 1 M and the 2 M LiTFSI electrolytes that the speciation (fractions of S_8^{2-}, S_6^{2-}, S_4^{2-}) of LiPS in the electrolyte changed as is revealed by UV–vis below.

Upon increasing the LiTFSI concentration to 4 M (Fig. 3c), the extraction rate of LiPSs species into solution significantly decreases under optical monitoring. At $t = 20$ min, only a small amount of

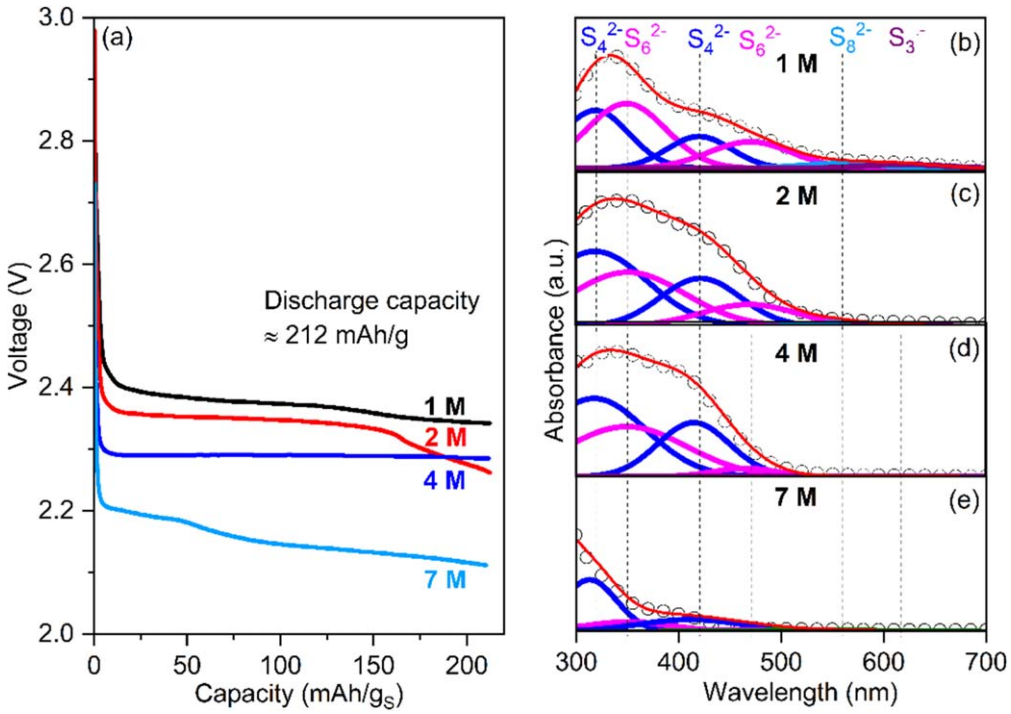

Figure 4. (a) Discharge curves of 1, 2, 4 and 7 M LiTFSI in DOL:DME (1:1 by vol.) at a current rate of C/30 corresponding to the region of the first plateau. (b)–(e) Deconvolution of absorbance UV–vis spectra of the different electrolyte concentrations into its Gaussian components: experimentally collected absorption spectra (open circle) shown for every 30th data points collected and used for fitting; the sum of all the Gaussian components is shown as the red curve.

Version of record at: https://doi.org/10.1149/1945-7111/ac8b3d

Table I. Diagram of Li–S batteries electrolyte systems with speciation and LiPS shuttling characteristics.[17,18]

Fully-Solvating Electrolyte (FSE)	Sparingly-Solvating Electrolyte (SSE)	Sparingly-Solvating with diluent (SSE-wD)
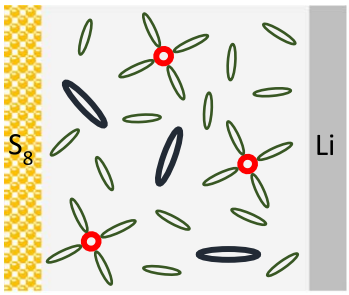	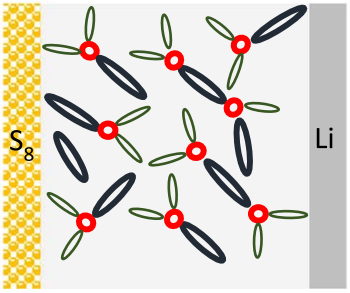	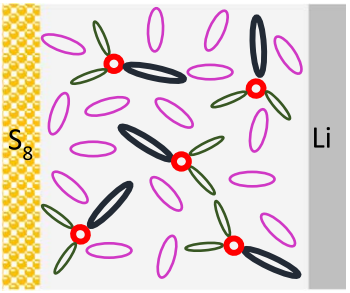
Dissolves LiPS $S_{8(s)} \rightarrow Li_2S_{8(l)} \rightarrow Li_2S_{6(l)} \rightarrow Li_2S_{4(s+l)} \rightarrow Li_2S_{2(s)} \rightarrow Li_2S_{(s)}$ Unsaturated polar solvent	Low dissolution of LiPS Early local supersaturation of LiPS $S_{8(s)} \rightarrow [Li_2S_{8(l)} \rightarrow Li_2S_{6(l)}]_{trans.} \rightarrow Li_2S_{4(s+l)} \rightarrow Li_2S_{2(s)}/Li_2S_{(s)}$ Saturated polar solvent Saturated non-polar solvent	Same properties as sparingly solvating Reduce viscosity Allows partial but minimal LiPS solubility
- Li^+ - Salt anion - Solvent - Diluent		

green-orange sulfur species emerges from the electrode; the electrolyte remains mostly clear. At $t = 1.5$ h, unlike the 2 M where a "geyser" plume is observed, the green-orange LiPS mixture in the 4 M electrolyte readily diffuses and spreads in solution clouding the electrolyte in a similar manner as the deep-orange sulfur species in the 1 M electrolyte. At the end of the 4 h discharge, the electrolyte at large adopts a green-orange coloring.

Near salt-saturation at 7 M LiTFSI in the DOL:DME (Fig. 3d), the electrolyte remains mostly clear past $t = 20$ min. Notable visual change in the electrolyte color is ascertained only past $t = 1.5$ h. By the end of the 4 h discharge a faint yellow coloring of the electrolyte is noted that is starkly less pronounced compared to the preceding color changes in the 1, 2, and 4 M electrolytes. As the salt concentration in the electrolyte is increased, the number of free ligand (lone pair of oxygen in DME and DOL) decreases resulting in decreased solvation of LiPS and thereby dissolution and crossover. We confirm this result in a coin cell with our electrode and electrolytes in Figs. S1a–S1c (available online at stacks.iop.org/JES/169/090518/mmedia) where capacity retention improves as LiTFSI concentration increases from 1 M to 2 M in DOL:DME. This further aligns with the literature results summarized in Fig. 1. Although it has been shown by Suo et al.[36] that when the concentration of the baseline electrolyte is increased, production of LiPSs from chemical (not electrochemical) disproportionation of Li_2S_8 is curtailed, the present work provides a unique visualization of the electrochemical conversion in situ adding insight into the diffusion behavior of the various LiPSs generated under current at steadily increasing concentration of lithium salt. For example, it is conceivable that self-sticking behavior of the soluble LiPS in the 2 M electrolyte may be more amenable to polysulfide trapping schemes[22–27] performed via electrode and separator modifications avoiding costly salt saturation of the electrolyte.

Furthermore, although SSE has the potential to improve the capacity retention and coulombic efficiency of LSBs due to its ability to limit LiPS crossover, its reaction kinetics and rate capability are affected. Figure 4a shows a systematic increase in discharge overpotential as the salt concentration increases. The average discharge voltage at the same C/30 current in the same glass cell configuration over the ~212 $mAh \cdot g^{-1}_{Sulfur}$ steadily decreased from ~2.38 V at 1 M to 2.34 V at 2 M to 2.29 V at 4 M to 2.15 V at 7 M. This is due to the increase in polarization as the salt concentration in the electrolyte increases as shown in the supporting information (Fig. S1d). The phenomenon is attributed to (i) reduced solubility of LiPSs which lowers sulfur mobility and exacerbates the electrochemical impact of the electrically-insulating nature of sulfur species, (ii) the reduction in electrolyte conductivity due to increased viscosity and ion crowding and (iii) more negative chemical potential of soluble polysulfides than insoluble polysulfides.[36] Electrochemical impedance spectroscopy in coin cells made with the 1 M and 2 M electrolytes are shown in Fig. S2 with the goal assessing the ohmic and kinetics effect independent of LiPS solubility (since EIS is a near-equilibrium technique). Before cycling, the bulk electrolyte and charge transfer resistances of the cell with 2 M electrolyte are 7.1 Ω and 233.71 Ω, respectively. In contrast, the bulk and charge transfer resistance of the cell with 1 M electrolyte are 4.9 Ω and 133.52 Ω respectively. The significant

Table II. Summary of UV–vis fits with estimated ratio of S_4^{2-} to S_6^{2-}.

Peak	S_4^{2-}	S_6^{2-}	S_4^{2-}	S_6^{2-}	S_8^{2-}	$S_3^{\cdot-}$
Position (nm)	320	350	420	470	560	617
1 M						
Area (%)	28	37	15	16	2.7	2.6
Ratio (S_4^{2-}/S_6^{2-})	0.76		0.94		—	—
2 M						
Area (%)	39	30	19	10	1.1	0.6
Ratio (S_4^{2-}/S_6^{2-})	1.3		1.9		—	—
4 M						
Area (%)	43	32	21	3	0.3	0.4
Ratio (S_4^{2-}/S_6^{2-})	1.34		7			
7 M						
Area (%)	100	30	45	4.4	2.3	1.3
Ratio (S_4^{2-}/S_6^{2-})	3.3		10.2		—	—

increase in the charge transfer resistance upon increase of concentration from 1 M to 2 M indicates a decrease in electrode kinetics. The slight increase in bulk electrolyte resistance confirms the idea of reduction in electrolyte ionic conductivity at concentrations above 1 M.

Ex-situ UV–vis spectra analysis.—The UV–vis spectra presented in Figs. 4b–4e show the approximate polysulfide composition in each electrolyte concentration upon discharge to ~212 mAh·g$^{-1}_{Sulfur}$. Again 212 mAh·g$^{-1}_{Sulfur}$ is the capacity range wherein main soluble LiPSs are produced.

We identify and deconvolute via Levenberg Marquardt fitting the UV–vis peaks of S_8^{2-} at 560 nm, S_6^{2-} at 470 nm and 350 nm, S_4^{2-} at 420 nm and 320 nm, $S_3^{\cdot-}$ at 617 nm as reported by Zou et al.[53] (UV bands assigned in 1 M LiTFSI in DOL:DME (1:1, by vol.)). Absorption spectra were decomposed into their approximate Gaussian components so that the contributions of each polysulfides species observed in each electrolyte can be estimated and compared in Table I.

In all cases, the 560 nm wavelength show negligible UV absorbance which indicates that S_8^{2-} is not detected; reduction of S_8^{2-} to shorter chain polysulfides occurs early in the discharge prior to reaching the 212 mAh·g$^{-1}_{Sulfur}$ at which the UV–vis was collected.[53] The area ratios of the peaks at ~320 nm to the peak at 350 nm assigned to S_4^{2-} and S_6^{2-} respectively change from 0.76 to 1.3 to 1.34 to 3.3 in Table II.

The area ratios of the peaks at ~420 nm to the peak at 470 nm assigned to S_4^{2-} and S_6^{2-} respectively also change from 0.94 to 1.9 to 7 to 10.2. A systematic increase of the ratio of S_4^{2-}/S_6^{2-} at 212 mAh·g$^{-1}_{Sulfur}$ is evident as the LiTFSI concentration increases from 1 M to 7 M. This shows that the reaction pathway in fully-solvating electrolytes permit longer residence time of more soluble, longer-chain polysulfides (in the form S_6^{2-} as opposed to S_4^{2-} at the 212 mAh·g$^{-1}_{Sulfur}$ point probed) leading to excessive polysulfide shuttling. When the concentration is increased to 7 M, attempts at fitting for the two peaks of S_6^{2-} was less reliable compared to the 4 M and below. Although both S_4^{2-} and S_6^{2-} were fitted in Fig. 4e, we note that successful fitting was also achieved by fitting just the two peaks assigned to S_4^{2-}. This suggests that S_6^{2-} species were not leaked in significant quantities into the electrolyte solvent likely due to the absence of free solvent molecules for solvation of long-chain polysulfides leading to accelerated conversion from S_8^{2-} down to S_4^{2-}, disallowing any appreciable build-up of soluble long chain polysulfides. These observations are in alignment with the color shift from deep-orange to faint yellow upon increase of the electrolyte LiTFSI concentration from 1 M to 7 M. The distinctly greater coulombic efficiency in SSEs seen in Fig. 2b compared to FSE is easily explained by the visual cell data combined with the quantified UV–vis; the supersaturation of long-chain polysulfides in sparingly-solvating 7 M electrolyte is reached early in the reaction (compared to dilute 1 M) leading to an essentially electrode-confined solid-state reaction that diminishes the polysulfide shuttle. With the more rapid conversion to shorter chain polysulfides (more electrons per product) in the higher concentration electrolytes, a smaller amount of the starting S_8 needs to be converted for the same capacity of 212 mAh·g$^{-1}_{Sulfur}$ which further aids in reducing the amount of LiPSs in the electrolytes.

It is worth noting, however, that even in salt-saturated, highly concentrated, sparingly-solvating DOL:DME, Li_2S_4 still shuttles at visually detectable levels (Figs. 3d, 4h) albeit more slowly into the electrolyte. This trickle LiPS-shuttle partially explains the fact that the nominally-improved 50th cycle retention estimated from literature review in Fig. 1a is still only ~70% on average in SSEs. Furthermore, as mentioned above, the kinetics of the reaction are adversely impacted by the increased salt concentration suggesting further remediation is needed. This challenge is the object of efforts under way in our laboratory.

Conclusions

In summary, we employ an optical operando lithium-sulfur cell and ex situ UV–vis spectroscopy to investigate soluble polysulfides speciation in fully and sparingly solvating LSB electrolytes. In the study, the color change and mobility pattern at increasing LiTFSI in DOL:DME electrolyte exhibit significant variations which highlight the impact of electrolyte on the dissolution, diffusion, and shuttling of lithium-polysulfides in lithium-sulfur batteries. Ex situ UV–vis spectroscopy in the different electrolyte systems reveal a shift towards shorter-chain polysulfides with increasing salt concentration, enabling reduced solvation. Fully solvating electrolytes solubilize polysulfides which is reflected favorably on the redox kinetics but leads to undesired excess shuttling of long-chain lithium polysulfides. In contrast, sparingly-solvating electrolytes solvate polysulfides only partially due to curtailed free solvent molecules; this minimizes the shuttling effect and conserves active material. However, resulting low lithium ion and sulfur-species mobility in the electrode and electrolyte negatively impact the redox kinetics, increasing discharge overpotential. An optimal electrolyte for LSBs could combine the attributes of these two electrolyte systems for a durable and efficient LSB.

Acknowledgments

This research was funded by University of Delaware faculty start-up support for Koffi Yao. The authors declare that the research was conducted in the absence of any commercial or financial relationships that could be construed as a potential conflict of interest. KPY is the principal investigator. GST performed the experiments and drafted the manuscript. MM did the fitting of the UV–vis spectra and interpretation of data. AR provided postdoctoral experimental guidance and suggestions during the experimentation phase.

ORCID

Gbenga S. Taiwo https://orcid.org/0000-0002-1659-9084
Mritunjay Mishra https://orcid.org/0000-0001-8394-6691
Koffi P. C. Yao https://orcid.org/0000-0003-4310-4347

References

1. M. Armand and J.-M. Tarascon, *Nature*, **451**, 652 (2008).
2. N. Angulakshmi and A. M. Stephan, *Frontiers in Energy Research*, **3**17 (2015).
3. J.-S. Lee, S. Tai Kim, R. Cao, N.-S. Choi, M. Liu, K. T. Lee, and J. Cho, *Adv. Energy Mater.*, **1**, 34 (2011).
4. Z. P. Cano, D. Banham, S. Ye, A. Hintennach, J. Lu, M. Fowler, and Z. Chen, *Nat. Energy*, **3**, 279 (2018).
5. P. G. Bruce, S. A. Freunberger, L. J. Hardwick, and J.-M. Tarascon, *Nat. Mater.*, **11**, 19 (2012).
6. J. W. Choi and D. Aurbach, *Nature Reviews Materials*, **1**, 16013 (2016).
7. X.-P. Gao and H.-X. Yang, *Energy Environ. Sci.*, **3**, 174 (2010).
8. J. B. Goodenough and Y. Kim, *Chem. Mater.*, **22**, 587 (2010).

9. B. Dunn, H. Kamath, and J.-M. Tarascon, *Science*, **334**, 928 (2011).
10. C. P. Grey and J. M. Tarascon, *Nat. Mater.*, **16**, 45 (2017).
11. S. Evers and L. F. Nazar, *Acc. Chem. Res.*, **46**, 1135 (2013).
12. X. Ji, K. T. Lee, and L. F. Nazar, *Nat. Mater.*, **8**, 500 (2009).
13. Y. Yang, G. Zheng, and Y. Cui, *Chem. Soc. Rev.*, **42**, 3018 (2013).
14. B. L. Ellis, K. T. Lee, and L. F. Nazar, *Chem. Mater.*, **22**, 691 (2010).
15. B. D. McCloskey, *J. Phys. Chem. Lett.*, **6**, 4581 (2015).
16. C.-W. Lee, Q. Pang, S. Ha, L. Cheng, S.-D. Han, K. R. Zavadil, K. G. Gallagher, L. F. Nazar, and M. Balasubramanian, *ACS Central Science*, **3**, 605 (2017).
17. L. Cheng, L. A. Curtiss, K. R. Zavadil, A. A. Gewirth, Y. Shao, and K. G. Gallagher, *ACS Energy Lett.*, **1**, 503 (2016).
18. Y. Liu, Y. Elias, J. Meng, D. Aurbach, R. Zou, D. Xia, and Q. Pang, *Joule*, **5**, 2323 (2021).
19. L. Fan, M. Li, X. Li, W. Xiao, Z. Chen, and J. Lu, *Joule*, **3**, 361 (2019).
20. C. Dong, W. Gao, B. Jin, and Q. Jiang, *iScience*, **6**, 151 (2018).
21. W. Zhang, S. Li, A. Zhou, H. Song, Z. Cui, and L. Du, *Molecules*, **26**, 6341 (2021).
22. G. Ai, Y. Dai, W. Mao, H. Zhao, Y. Fu, X. Song, Y. En, V. S. Battaglia, V. Srinivasan, and G. Liu, *Nano Lett.*, **16**, 5365 (2016).
23. Z. Xiao, Z. Yang, L. Wang, H. Nie, M. Zhong, Q. Lai, X. Xu, L. Zhang, and S. Huang, *Adv. Mater.*, **27**, 2891 (2015).
24. X. Li et al., *Nano Lett.*, **16**, 3545 (2016).
25. Y. Tsao, H. Gong, S. Chen, G. Chen, Y. Liu, T. Z. Gao, Y. Cui, and Z. Bao, *Adv. Energy Mater.*, **11**, 2101449 (2021).
26. M. Yu, J. Ma, H. Song, A. Wang, F. Tian, Y. Wang, H. Qiu, and R. Wang, *Energy Environ. Sci.*, **9**, 1495 (2016).
27. M. Yu, W. Yuan, C. Li, J.-D. Hong, and G. Shi, *J. Mater. Chem. A*, **2**, 7360 (2014).
28. J.-Q. Huang, Q. Zhang, H.-J. Peng, X.-Y. Liu, W.-Z. Qian, and F. Wei, *Energy Environ. Sci.*, **7**, 347 (2014).
29. W. Zhu, Z. Zhang, J. Wei, Y. Jing, W. Guo, Z. Xie, D. Qu, D. Liu, H. Tang, and J. Li, *J. Membr. Sci.*, **597**, 117646 (2020).
30. J.-Q. Huang, Q. Zhang, and F. Wei, *Energy Storage Mater.*, **1**, 127 (2015).
31. Y. Li, Z. Li, C. Zhou, X. Liao, X. Liu, X. Hong, X. Xu, Y. Zhao, and L. Mai, *Chem. Eng. J.*, **422**, 130107 (2021).
32. K. Ueno, J.-W. Park, A. Yamazaki, T. Mandai, N. Tachikawa, K. Dokko, and M. Watanabe, *The Journal of Physical Chemistry C*, **117**, 20509 (2013).
33. Q. Li, J. Chen, L. Fan, X. Kong, and Y. Lu, *Green Energy & Environment*, **1**, 18 (2016).
34. J. Gao, M. A. Lowe, Y. Kiya, and H. D. Abruna, *The Journal of Physical Chemistry C*, **115**, 25132 (2011).
35. H. Wang et al., *Nano Energy*, **76**, 105041 (2020).
36. L. Suo, Y.-S. Hu, H. Li, M. Armand, and L. Chen, *Nat. Commun.*, **4**, 1481 (2013).
37. K. Dokko et al., *J. Electrochem. Soc.*, **160**, A1304 (2013).
38. E. S. Shin, K. Kim, S. H. Oh, and W. il Cho, *Chem. Commun.*, **49**, 2004 (2013).
39. A. Shyamsunder, W. Beichel, P. Klose, Q. Pang, H. Scherer, A. Hoffmann, G. K. Murphy, I. Krossing, and L. F. Nazar, *Angew. Chem. Int. Ed.*, **56**, 6192 (2017).
40. Q. Pang, A. Shyamsunder, B. Narayanan, C. Y. Kwok, L. A. Curtiss, and L. F. Nazar, *Nat. Energy*, **3**, 783 (2018).
41. K. A. See, H.-L. Wu, K. C. Lau, M. Shin, L. Cheng, M. Balasubramanian, K. G. Gallagher, L. A. Curtiss, and A. A. Gewirth, *ACS Appl. Mater. Interfaces*, **8**, 34360 (2016).
42. M. Cuisinier, P.-E. Cabelguen, B. D. Adams, A. Garsuch, M. Balasubramanian, and L. F. Nazar, *Energy Environ. Sci.*, **7**, 2697 (2014).
43. S. Drvarič Talian, S. Jeschke, A. Vizintin, K. Pirnat, I. Arčon, G. Aquilanti, P. Johansson, and R. Dominko, *Chem. Mater.*, **29**, 10037 (2017).
44. J. Jiang, Q. Fan, H. Liu, S. Chou, K. Konstantinov, and J. Wang, *ACS Appl. Mater. Interfaces*, **13**, 28405 (2021).
45. J.-W. Park, K. Yamauchi, E. Takashima, N. Tachikawa, K. Ueno, K. Dokko, and M. Watanabe, *The Journal of Physical Chemistry C*, **117**, 4431 (2013).
46. F. Wu, F. Chu, G. A. Ferrero, M. Sevilla, A. B. Fuertes, O. Borodin, Y. Yu, and G. Yushin, *Nano Lett.*, **20**, 5391 (2020).
47. C. Weller, S. Thieme, P. Härtel, H. Althues, and S. Kaskel, *J. Electrochem. Soc.*, **164**, A3766 (2017).
48. M. Rohde, P. Eiden, V. Leppert, M. Schmidt, A. Garsuch, G. Semrau, and I. Krossing, *ChemPhysChem*, **16**, 666 (2015).
49. C. Weller, J. Pampel, S. Dörfler, H. Althues, and S. Kaskel, *Energy Technology*, **7**, 1900625 (2019).
50. J. T. Lee, Y. Zhao, S. Thieme, H. Kim, M. Oschatz, L. Borchardt, A. Magasinski, W.-I. Cho, S. Kaskel, and G. Yushin, *Adv. Mater.*, **25**, 4573 (2013).
51. F. Huang, L. Gao, Y. Zou, G. Ma, J. Zhang, S. Xu, Z. Li, and X. Liang, *J. Mater. Chem. A*, **7**, 12498 (2019).
52. M. Yanagi, K. Ueno, A. Ando, S. Li, Y. Matsumae, J. Liu, K. Dokko, and M. Watanabe, *J. Electrochem. Soc.*, **167**, 070531 (2020).
53. Q. Zou and Y.-C. Lu, *The Journal of Physical Chemistry Letters*, **7**, 1518 (2016).
54. Q. He, A. T. S. Freiberg, M. U. M. Patel, S. Qian, and H. A. Gasteiger, *J. Electrochem. Soc.*, **167**, 080508 (2020).
55. M. U. M. Patel and R. Dominko, *ChemSusChem*, **7**, 2167 (2014).
56. Q. He, Y. Gorlin, M. U. M. Patel, H. A. Gasteiger, and Y.-C. Lu, *J. Electrochem. Soc.*, **165**, A4027 (2018).
57. G. Zhang, H.-J. Peng, C.-Z. Zhao, X. Chen, L.-D. Zhao, P. Li, J.-Q. Huang, and Q. Zhang, *Angew. Chem. Int. Ed.*, **57**, 16732 (2018).
58. S. Huang, Y. von Lim, X. Zhang, Y. Wang, Y. Zheng, D. Kong, M. Ding, S. A. Yang, and H. Y. Yang, *Nano Energy*, **51**, 340 (2018).
59. Y. Song, W. Zhao, L. Kong, L. Zhang, X. Zhu, Y. Shao, F. Ding, Q. Zhang, J. Sun, and Z. Liu, *Energy Environ. Sci.*, **11**, 2620 (2018).
60. W. Zhu et al., *Sustainable Energy & Fuels*, **1**, 737 (2017).
61. M. Hagen, P. Schiffels, M. Hammer, S. Dörfler, J. Tübke, M. J. Hoffmann, H. Althues, and S. Kaskel, *J. Electrochem. Soc.*, **160**, A1205 (2013).
62. C. Dillard, A. Singh, and V. Kalra, *The Journal of Physical Chemistry C*, **122**, 18195 (2018).
63. N. Saqib, C. J. Silva, C. M. Maupin, and J. M. Porter, *Appl. Spectrosc.*, **71**, 1593 (2017).
64. Y. Sun, Z. W. Seh, W. Li, H. Yao, G. Zheng, and Y. Cui, *Nano Energy*, **11**, 579 (2015).
65. M. Sadd, S. de Angelis, S. Colding-Jørgensen, D. Blanchard, R. E. Johnsen, S. Sanna, E. Borisova, A. Matic, and J. R. Bowen, *Adv. Energy Mater.*, **12**, 2103126 (2022).